Tracking bacteria at high density with FAST, the Feature-Assisted Segmenter/Tracker

Oliver J. Meacock[1,2,3,*], William M. Durham[1,2,†]

[1] Department of Zoology, University of Oxford, Oxford, United Kingdom
[2] Department of Physics and Astronomy, University of Sheffield, Sheffield, United Kingdom
[3] Department of Fundamental Microbiology, University of Lausanne, Lausanne, Switzerland

Abstract

Most bacteria live attached to surfaces in densely-packed communities[1,2]. While new experimental and imaging techniques are beginning to provide a window on the complex processes that play out in these communities, resolving the behaviour of individual cells through time and space remains a major challenge. Although a number of different software solutions have been developed to track microorganisms[3–8], these approaches typically rely on a large number of user-defined parameters that must be carefully tuned to effectively track cells. Testing a single set of parameters can take hours to days depending on the size of the dataset, making iterative rounds of optimisation impractical. To overcome these limitations, we have developed FAST, the Feature-Assisted Segmenter/Tracker, which uses unsupervised machine learning to optimise tracking. Our approach, rooted in information theory, largely eliminates the need for users to iteratively adjust parameters manually and make qualitative assessments of the resulting cell trajectories. Instead, FAST measures multiple distinguishing "features" for each cell and then autonomously quantifies the amount of unique information each feature provides. We then use these measurements to determine how data from different features should be combined to minimize tracking errors. Comparing our algorithm with a naïve approach that uses cell position alone revealed that FAST produces 4 to 10 times fewer tracking errors. The modular design of FAST combines our novel tracking method with tools for segmentation, extensive data visualisation, lineage assignment, and manual track correction. It is also highly extensible, allowing users to extract custom information from images and seamlessly integrate it into downstream analyses. FAST therefore enables high-throughput, data-rich analyses with minimal user input. It has been released for use in either Matlab or as a compiled stand-alone application, and is available at https://bit.ly/3vovDHn, along with extensive tutorials and detailed documentation.

Introduction

Time-lapse microscopic imaging and automated cell tracking has led to many fundamental advances in our understanding of how microorganisms sense and respond to their environment. While many studies have focused on the movement of planktonic bacteria at relatively low densities, many behaviours – including collective movement[9,10], combat[11], sharing of public goods[12] and genetic exchange[13] – typically only occur in the closely-packed assemblages in which most microbes live. These dense communities are often studied in the laboratory using confluent monolayers of cells, which are much easier to image than three-dimensional aggregations. One method to generate such monolayers is to confine cells with a slab of agarose or polyacrylamide to form an interstitial colony[9,14–16], while more advanced microfluidic techniques[17] can also be used to confine cells to a single plane while allowing for more precise control over their chemical environment (Fig. 1a). Monolayers can also form in thin films of fluid, including those arising naturally during bacterial swarming motility[10] and in assays used to study mixing induced by flagellar motility[18]. Regardless of the origin of the monolayer

*oliver.meacock@unil.ch
†w.m.durham@sheffield.ac.uk

however, investigators face the same technical challenges when tracking densely packed cells using phase-contrast, brightfield and/or epi-fluorescence microscopy (Fig. 1b).

Tracking solitary cells at low density is relatively straightforward, and basic tracking algorithms that use cell position alone often produce excellent results. However, tracking cells that are densely packed together is notoriously difficult because the spacing between neighbouring cells becomes similar to the distance cells move between frames. These problems are exacerbated by cell motility. While some species of bacteria are non-motile at high density and spread slowly only via cell division and the secretion of surfactants[15,17], emergent patterns of collective motility driven by twitching[9], swarming[10] and gliding[19] further complicate tracking by rapidly changing the positions of cells. Consequently, dense, motile communities must be imaged at high framerates for tracking to be feasible, such that a typical experiment requires a timeseries of hundreds or thousands of images. The large size of imaging datasets, combined with the large number of cells within each image, means that the computational time required for cell tracking is often one of the main bottlenecks in a researcher's workflow. This can be compounded if tracking must be repeated multiple times to optimise tracking parameters.

A basic nearest-neighbour tracking algorithm compares the coordinates of cell centroids between subsequent frames and build trajectories by connecting those centroids that are closest together between subsequent time points. More advanced algorithms leverage additional cell characteristics or "features" to distinguish cells from one another, including metrics that measure cell shape, orientation, fluorescence levels and patterns of previous movement[3,21–23]. However, incorporating these additional feature measurements introduces a new problem, namely how to efficiently combine the information from different features to optimise tracking performance. In some software packages (e.g. MicrobeJ[3]), this requires the user to manually choose a large number of parameters and make qualitative judgements of the trajectories that result from each set of parameters. The combinatorial explosion in the number of possible parameters, the fact that a single parameter set can require many hours to test, and the lack of a rigorous way to compare the tracking results across different parameter sets, means that parameter optimisation in such a tracking algorithm is typically a highly iterative, time-consuming process.

A related problem is the fact that properties of bacteria within collectives are highly dynamic, changing at both the individual level and population level over time. For example, fluorophores can accumulate within cells or bleach, while cell movement can speed up or slow down due to the secretion of extracellular factors or changes in gene expression[24,25]. In addition, the overall density of cells often increases over time as a result of cell division. This variability means that an algorithm optimised to track cells at the beginning of an experiment might struggle at later timepoints. Furthermore, experimental issues - such as changes in illumination, focus, or shifts in the field of view caused by thermal drift - can cause an abrupt deterioration of tracking accuracy. Knowing when tracking accuracy has deteriorated to an unacceptable level often lacks a rigorous basis and requires the output of tracking software to be carefully validated by eye, typically infeasible for high-throughput datasets.

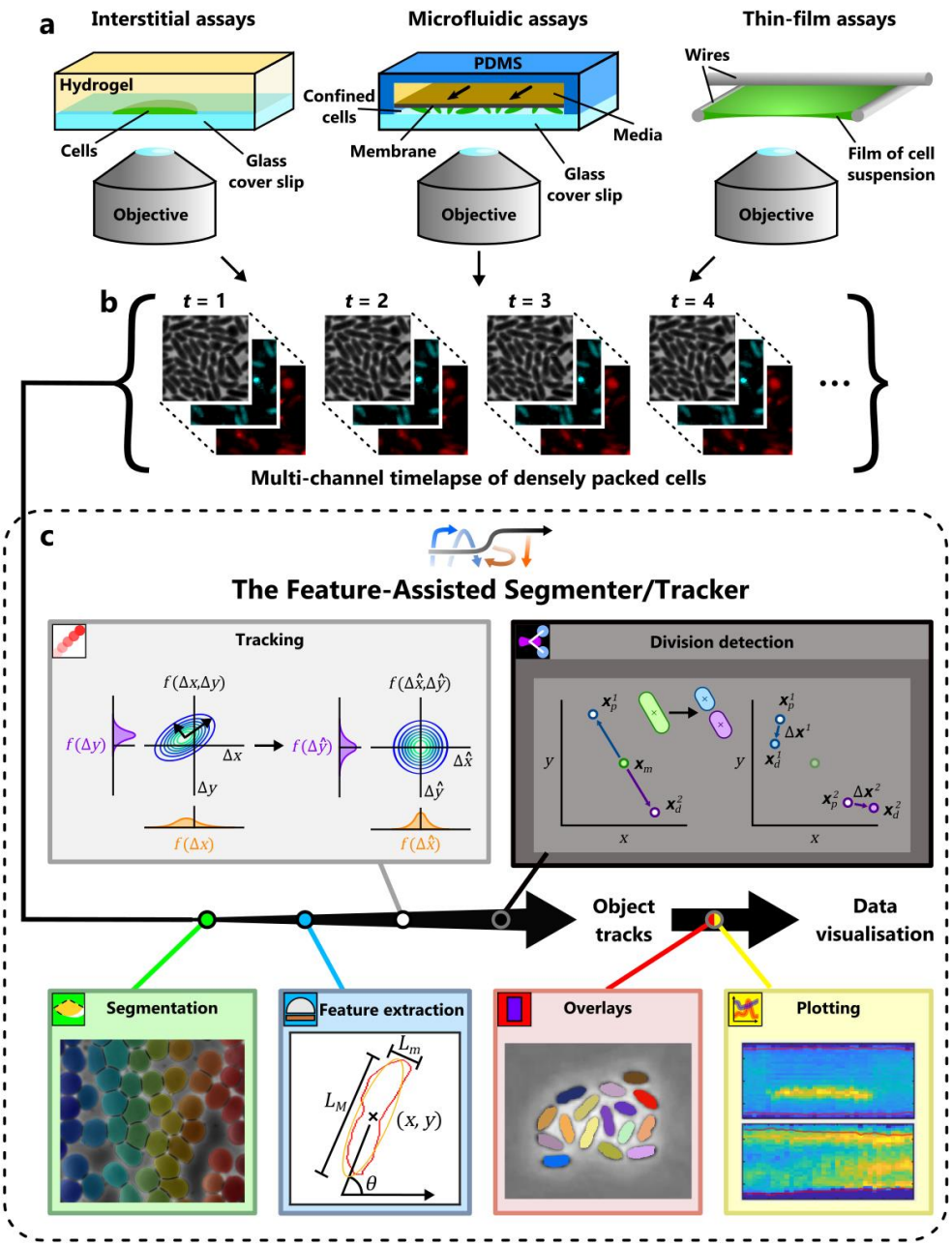

Fig. 1 | Analysis of high-density datasets using FAST's modular framework. *(a) While bacteria naturally form monolayers in some environments[10], a number of different assays are used to physically confine cells to a plane in laboratory experiments. Among these are interstitial colonies[9,14–16], microfluidic devices that trap cells between two solid boundaries[17], and experimental assays that confine cells to a thin film of liquid[18]. (b) These experiments are typically imaged using automated microscopy systems capable of collecting images in both transmitted light and fluorescent channels at specified time points. (c) FAST analyses these imaging datasets in six separate modules, each of which is used in sequence (see text). A complete specification of each module is provided in the Supplementary Information.*

In this paper, we discuss a new approach that uses unsupervised machine learning to improve the fidelity of tracking. Our system automatically measures the statistical properties of each feature over time and then uses this data to dynamically change the relative weighting of each feature based on the information it can contribute to solving the tracking problem. It also provides users with a metric of the expected accuracy of the resulting cell trajectories, alerting them to sections of datasets that may need to be omitted from subsequent analyses. This tracking algorithm is combined with robust

segmentation, feature extraction, lineage analysis and visualisation routines to make up FAST, the Feature-Assisted Segmenter/Tracker. FAST has been released as open-source software which can be run either directly within Matlab or as a stand-alone application, and has already been used in a number of publications to accurately analyse densely-packed bacterial monolayers[9,16,26,27].

In the following sections, we discuss the design approach and general structure of FAST, and then illustrate the utility of our novel cell tracking approach using synthetic datasets. Next, we discuss three case studies that illustrate the versatility of FAST, including: 1) tracking of twitching *P. aeruginosa* cells in a 2D monolayer, 2) lineage analysis of an *E. coli* colony, and 3) automated analysis of the Type 6 Secretion System (T6SS) in a co-culture of *P. aeruginosa* and *V. cholerae*. While these case studies focus on densely packed bacteria, FAST can also be used to analyse other types of biological samples (*e.g.* Fig. S1g-i).

Design criteria

Following an extensive review of existing cell tracking software packages[3–8] and testing them on images of densely packed bacterial monolayers, we established several design criteria for FAST:

1. **Modular construction:** Many existing tracking software packages use single GUI that contains all of their functionality. While this approach offers some advantages, the complexity of the resulting interface can be daunting to the novice user. Instead of this integrated approach, we decided to split FAST into several distinct modules, each with its own layout and workflow. The unique layout of each module within FAST allows users to visualise the results of each stage and directly optimise each user-defined parameter at intermediate points within the analysis, rather than having to rely solely on the final output.
2. **Rapid feedback:** Many software packages require the entire dataset to be analysed before the quality of analysis can be assessed. This can render the manual optimisation of analytical parameters impractical, as large datasets can take hours or even days to process. One of the critical goals of FAST was therefore to allow users to quickly analyse small subsets of their data and to provide immediate visual feedback on these analyses. Users can use these capabilities to rapidly optimise parameter sets. We also provide tools to rapidly identify portions of a timeseries where the tracking accuracy is diminished, allowing users to remove them from further analysis to reduce wasted computational effort.
3. **Minimizing the number of user-defined parameters:** As more and more features are incorporated into a tracking algorithm, the number of analytical parameters can become too large to optimise manually using an iterative approach. To avoid this, our machine learning-based tracking optimally integrates information across an arbitrary number of features. By calculating the statistical properties of each feature and automatically normalising them relative to one another, the user only needs to optimise a single tracking parameter.
4. **Extensibility:** Although many of the existing software packages we tested are powerful, in many cases they were designed to perform a specific task (e.g. lineage reconstruction[5] or measurement of extracellular structures[28,29]). FAST provides an extensible framework to test diverse hypotheses by facilitating the measurement of novel cell features and allowing custom analyses to be integrated into its pipeline. New features can be specified by users via a short script, while the results of novel custom analyses can easily be imported for visualisation with FAST. For example, users can use custom features (like cell shape or the localization pattern of a particular fluorescent protein) to assign trajectories to distinct populations (representing, for example, different bacterial species).

The FAST analysis pipeline

Our design criteria were used to develop the FAST pipeline, which consists of six modules that are used in sequence (Fig. 1c). First, the Segmentation module is used to identify the boundaries of individual cells, typically using brightfield or phase-contrast images. Next, the Feature Extraction module measures a range of different cell properties such as position, size and fluorescence intensity (potentially in multiple channels) using the previously extracted segmentation as a basis. The Tracking module employs our machine learning process to quantify the information associated with each feature and then calculates the relative weighting of each feature to maximise tracking fidelity. If required, a manual validation and correction sub-module also allows the user to correct any mistakes made by the tracking algorithm. The optional Division Detection module uses a closely related machine learning process to assign daughter cells to mother cells following cell division events. Two separate modules can finally be used to visualise the output of FAST: the Overlay module plots trajectories and/or the results of analyses over the top of the original images, while the Plotting module contains a range of different options to visualise extracted data.

The FAST GUI guides the user through the process of analysing a single dataset. However, many applications require a large number of imaging datasets to be analysed using consistent settings. To automate this, we have implemented a batch-processing tool called doubleFAST. Once a user has performed an analysis on a single dataset using the FAST GUI, doubleFAST can then read the settings used during this initial run and automatically apply them to any number of additional datasets. This allows data from multiple experiments to be processed with minimal amounts of additional user input and ensures each has been analysed using consistent settings.

Finally, we have implemented a post-processing toolbox, which contains scripts and functions to perform a number of different tasks on FAST's output. These allow, among other things, conversion of track data to other file formats, automated detection of different genotypes, and the annotation of events such as reversals in movement direction. Users of FAST can suggest new additions to this toolbox so they can be used by the wider community.

FAST's tracking algorithm

One of FAST's principal innovations is its new tracking algorithm, which automatically determines how to best combine data from a variety of different cell features to improve tracking fidelity. Although previous tracking software packages have had the option to incorporate cell characteristics other than position in their tracking routines[21,23], FAST uses a conceptual framework based on information theory that optimises this process, increasing both the power and convenience of this approach. In this section we provide a high-level overview of our main innovations and how they impact the tracking process. For more detailed derivations and explanations, please refer to section 2.4 of the Supplementary Information.

Our approach to the tracking problem is based on measurements of the amount of information that can be used to assign links between objects in subsequent frames, a measurement we call the

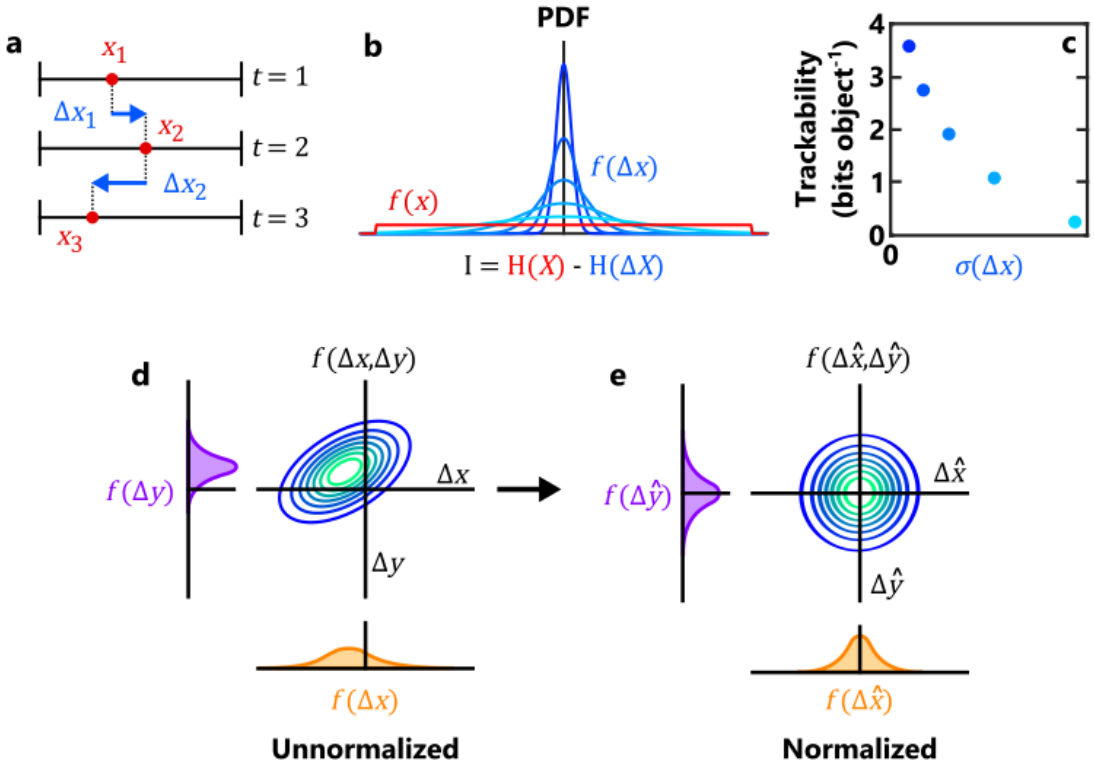

Fig. 2 | An information-theoretic framework for automated object tracking. *(a) For illustrative purposes, we consider here a theoretical dataset in which an object is characterised using a single feature, its position along the x-axis. The object's position at three successive timepoints is denoted x_1, x_2, x_3 (red circles), while the displacements are denoted $\Delta x_1, \Delta x_2$ (blue arrows). We assume that feature displacements are drawn from a Normal distribution $f(\Delta x)$, while the instantaneous object position (independent of knowledge of other timepoints) is drawn from a separate Uniform distribution $f(x)$ (b). The information content I of the feature is then calculated as the difference in the entropies of the two distributions, $H(X)$ and $H(\Delta X)$, and represents our increase in certainty about the position of the object at time $t+1$ given knowledge about its position at time t. The trackability quantifies the total amount of information measured for each object, which increases when $f(\Delta x)$ exhibits less variability relative to $f(x)$. (c) Trackability decreases when the distribution of $f(\Delta x)$ is broader (i.e. the feature becomes more "noisy"). Here the different colours correspond to the different distributions of $f(\Delta x)$ shown in panel b. d,e) Illustration of the feature normalization process for two features. In both d and e, the central plot indicates the joint distribution of a pair of feature displacements, while the left and bottom plots indicate the corresponding marginal distributions. In (d), the random variables representing the unnormalized frame-frame displacements of the two features - ΔX and ΔY - are correlated and displaced from the origin. Using the joint distribution's covariance matrix $\Sigma(\Delta \boldsymbol{x})$ and mean vector $\boldsymbol{\mu}(\Delta \boldsymbol{x})$, the feature space is transformed such that the resulting joint distribution of feature displacements $f(\Delta\hat{x}, \Delta\hat{y})$ is zero-centred and isotropic (e), ensuring that each feature exhibits an equivalent amount of stochastic variation between frames.*

"trackability". This trackability score provides an integrated measure of how accurately we can follow objects from frame to frame, and due to its grounding in information theory has certain desirable properties such as the additivity of contributions from statistically independent features[30,31]. Measuring the trackability over time therefore provides users with a tool to predict when tracking will be stable and robust, as well as flagging portions of a dataset that might yield spurious trajectories. We define trackability in the following paragraphs and then illustrate how this metric is used in practice in our first case study.

We begin by assuming that *N* different features are measured for each object. An object's features can be expressed as a vector $\boldsymbol{x}_t^i$ with *N* elements, where the object index is denoted as i and time is denoted as t. Changes in an objects' features over time – corresponding to, for example, translational movement or changes in fluorescence intensity – therefore generate a trajectory through the *N*-dimensional feature space. The goal of our tracking algorithm is to reconstruct each object's trajectory

from the cloud of individual data points resulting from the segmentation and measurement of objects in each image. As previously noted, individuals in high-density and high-motility systems can easily move further than the typical cell-cell separation between frames, making it difficult to reconstruct their trajectories from positional information alone. By including additional features in the tracking framework, we expand the feature space from these two spatial dimensions to *N* feature dimensions, creating new axes along which one can potentially discriminate neighbouring individuals from each other.

The trackability metric provides an estimate of how distinguishable trajectories are from each other in the feature space, and therefore how accurate tracking is likely to be. Unpredictable movement of objects tends to reduce trackability, while trackability increases if the features sample a wider range of values (*i.e.* if they have a larger dynamic range). To formalise this, we model an object's instantaneous position in feature space as the random vector $\boldsymbol{X}_t$ and the change in this position between subsequent images as the random vector $\Delta\boldsymbol{X}_t$. The distribution $f(\boldsymbol{x})$ is then the probability density function (PDF) representing the chance of finding a randomly selected object at a particular position $\boldsymbol{x}$ in the absence of additional information (specifically, the position of the object at prior timepoints), while the distribution $f(\Delta\boldsymbol{x})$ represents the stochastic change in an object's position in feature space between sequential timepoints. We estimate $f(\Delta\boldsymbol{x})$ by assuming that the motion of an object through feature space can be modelled as a Gaussian random walk. Explicitly, we assume that the feature vector $\boldsymbol{x}_{t+1}^i$ of an object at frame $t+1$ can be written in terms of its prior feature vector $\boldsymbol{x}_t^i$ as:

$$\boldsymbol{x}_{t+1}^i = \boldsymbol{x}_t^i + \Delta\boldsymbol{X}_t, \tag{1}$$

where $\Delta\boldsymbol{X}_t$ is modelled as a multivariate normal $\mathcal{N}(\boldsymbol{\mu}_t(\Delta\boldsymbol{x}), \Sigma_t(\Delta\boldsymbol{x}))$, and $\boldsymbol{\mu}_t(\Delta\boldsymbol{x})$ and $\Sigma_t(\Delta\boldsymbol{x})$ are respectively the mean vector and covariance matrix of the set of frame-frame feature displacements $\{\Delta\boldsymbol{x}_t\}$. We can similarly characterise $f(\boldsymbol{x})$ using the covariance matrix of the raw object locations, $\Sigma_t(\boldsymbol{x})$. While we can estimate $\Sigma_t(\boldsymbol{x})$ directly from static snapshots as the covariance of the set of feature vectors $\{\boldsymbol{x}_t\}$, resolving $\{\Delta\boldsymbol{x}_t\}$ and subsequently $\boldsymbol{\mu}_t(\Delta\boldsymbol{x})$ and $\Sigma_t(\Delta\boldsymbol{x})$ requires a putative set of cell trajectories, which in our algorithm are obtained via a preliminary round of tracking that uses a simple nearest-neighbour approach. These statistics are robust to small numbers of tracking errors, allowing us to train our model using this relatively low-fidelity tracking approach.

From these measurements, we estimate the amount of information available for assigning objects between frames by calculating the difference between the entropies for the two distributions, $\mathrm{H}(\boldsymbol{X})$ and $\mathrm{H}(\Delta\boldsymbol{X})$[31,32]. The trackability r_t in bits object^{-1} is then given as:

$$r_t = \frac{1}{2}\log_2\left(\frac{|\Sigma_t(\boldsymbol{x})|}{|\Sigma_t(\Delta\boldsymbol{x})|}\right) + \frac{N}{2}\log_2\left(\frac{6}{\pi e}\right) - \log_2(n_{o,t}), \tag{2}$$

where $n_{o,t}$ is the total number of objects present at time t and $|\cdot|$ denotes the determinant of the contents.

To illustrate the trackability metric, we consider the case of a single object with a single feature, for example its position in space along a single axis, x (Fig. 2a-c). This simplifies Eq. (2) to:

$$r_t = \frac{1}{2}\log_2\left(\frac{\sigma_t(x)^2}{\sigma_t(\Delta x)^2}\right) + \frac{1}{2}\log_2\left(\frac{6}{\pi e}\right), \tag{3}$$

where $\sigma_t(x)$ and $\sigma_t(\Delta x)$ denote the standard deviation of their respective distributions. As expected, one observes a larger trackability score when the distribution of feature displacements, $f(\Delta x)$, is more

212 sharply peaked relative to the distribution of $f(x)$ (Fig. 2b,c). *i.e.* when the typical distance an object
213 moves between frames is small compared to the range of values of x. If the trackability score is
214 sufficiently large, the risk that two objects move close to one another and become difficult to
215 distinguish is small. Intuitively, the precision of tracking will increase as (*i*) the size of the random
216 fluctuations in feature space decreases, (*ii*) the number of objects within a frame decreases, and (*iii*)
217 the total size of the feature space the objects occupy (*i.e.* their dynamic ranges) increases. By taking
218 these multiple factors into account, r_t represents an integrated measurement of the risk that a given
219 object will be incorrectly linked to a different object in a subsequent frame.

220 In addition to calculating the trackability, $\boldsymbol{\mu}_t(\Delta\boldsymbol{x})$ and $\Sigma_t(\Delta\boldsymbol{x})$ are also used to perform what we call
221 "feature normalization". This transformation converts the raw feature space $\boldsymbol{x}$ to a normalized feature
222 space $\hat{\boldsymbol{x}}$ with a corresponding displacement distribution $f(\Delta\hat{\boldsymbol{x}})$ that is isotropic and zero-centred (Fig.
223 2d), thus ensuring that the stochastic variation observed within each component of $\hat{\boldsymbol{x}}$ is equal and that
224 any predictable motion in the feature space (e.g. a gradual increase in cell length due to growth, or a
225 reduction in fluorescent intensity due to photobleaching) is accounted for. The metric of this
226 transformed space is the Mahalanobis distance, a dimensionless measure of how reliably we can
227 predict where an object will appear in the feature space at the next time point under the assumptions
228 of our statistical framework. By providing an equitable way to combine data from different features
229 together, this metric allows us to more accurately distinguish correct from incorrect putative links.
230 Large distances between sequential timepoints in this space indicate a discrepancy between the
231 predicted and observed location of an object in the next frame, and so suggest that the input data
232 must be erroneous - for example, because an object was mis-segmented a single frame. In contrast to
233 previous approaches where feature weightings have to be selected or measured manually[21], feature
234 normalization allows one to automatically optimise the contribution of multiple features without any
235 additional user input.

236 Finally, we use these statistical measurements to also calculate the adaptive tracking threshold, which
237 automatically adjusts the stringency of the algorithm that links objects together based on how much
238 information is available in each frame. While a larger fraction of putative links are accepted when
239 information is relatively plentiful, only the highest certainty links are accepted when information is
240 more limited. This dynamic adjustment of the link threshold thus allows FAST to maximise the number
241 trajectories in less challenging tracking conditions (*e.g.* slow-moving cells at low density) while
242 minimizing the number of spurious links in more challenging conditions (*e.g.* fast-moving cells at high
243 density).

244 Validating the methodology of FAST using ground-truthed datasets

245 To demonstrate the functionality of our tracking algorithm and to illustrate how using multiple
246 features can enhance accuracy, we used a previously described self-propelled rod (SPR) model [9,33] to
247 generate synthetic data sets that simulate bacteria collectively moving at high-density (Fig. 3a). In
248 these simulations, cells are modelled as stiff, mutually repulsive rods that are propelled by a constant
249 force (Methods). This model has been shown to closely approximate bacterial collectives that propel
250 themselves using either flagella or type IV pili, where steric interactions between neighbouring cells
251 generate complex emergent collective behaviours[9,33]. Importantly, this approach allows us to
252 independently control each of the different properties of the system, allowing us to test FAST on a
253 large number of qualitatively different datasets and to compare the results with a known ground truth.

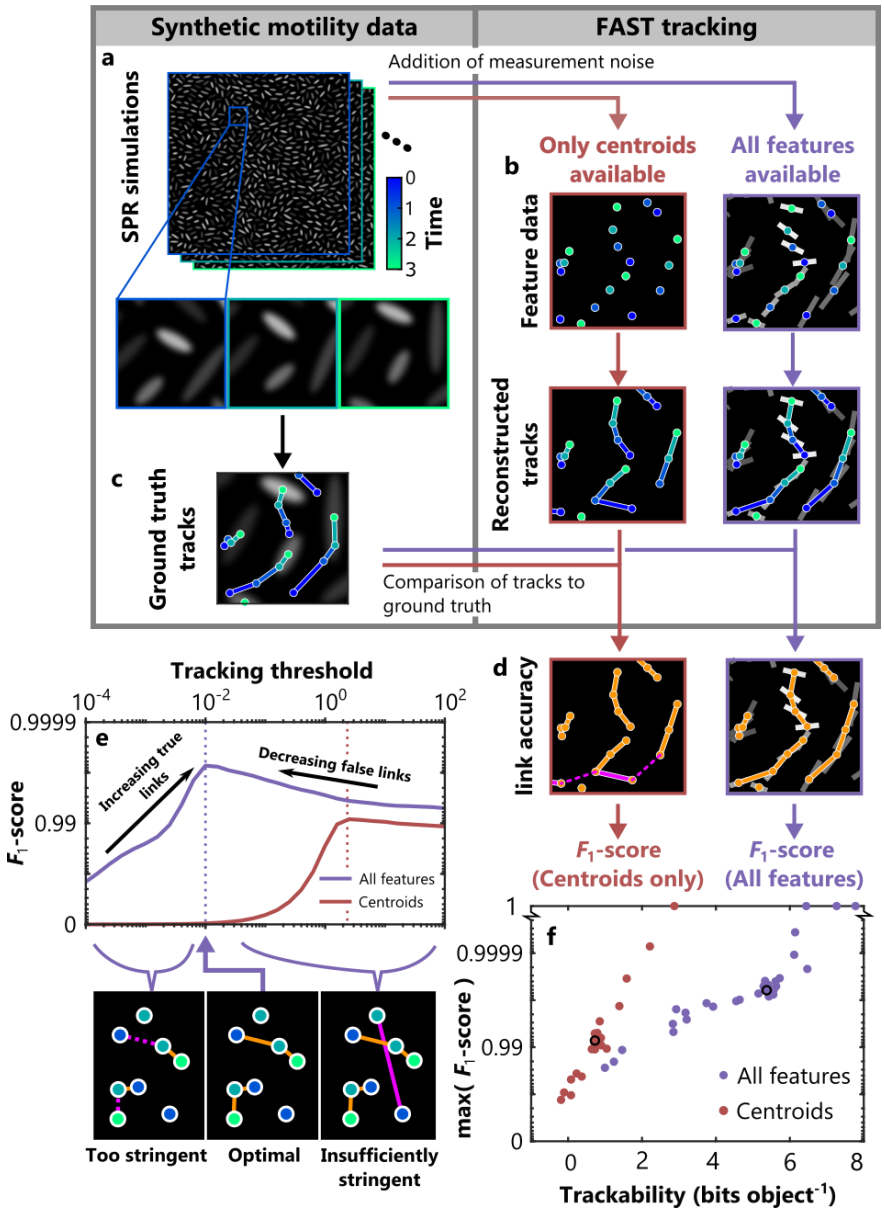

Fig. 3 | Validating FAST using synthetic data from a simulation of collective bacterial motility. *(a) We used a self-propelled rod (SPR) model to generate noisy datasets with a verified ground truth. We then performed cell tracking with FAST using either only a single feature (the rod's centroid at sequential timepoints; brown) or using a suite of different features (rod centroid, length, orientation and simulated fluorescence intensity; purple). Comparison of the reconstructed trajectories from FAST (b) with the ground truth data (c) allowed us to identify the errors made by the tracking algorithm (d). Errors were split into two categories: links made between objects that were incorrect ('false positives', solid magenta lines), and links between objects that were missed ('false negatives', dashed magenta lines). We also calculated the number of correct links made in each case ('true positives', solid orange lines). From these counts, we evaluated the performance of the tracking algorithm by calculating the F_1-score (main text). (e) The value of this F_1-score depends on a user-defined parameter, the tracking threshold. To objectively compare the results from the tracking algorithm when run on datasets with different properties, we calculated the tracking threshold that generated the largest F_1-score for a given dataset and used this score in subsequent analyses. (f) Including all feature information substantially and consistently improved tracking performance compared to when only object positions were used (see also Extended Data Fig. 2). Furthermore, we found that our trackability metric was an excellent predictor of tracking accuracy for a given set of features, suggesting that it can be used to estimate the accuracy of the algorithm even when a ground truth is not available. In the different simulations we varied rod density, propulsive force, and framerate, as well the amount of noise in the measurement of position, length and fluorescence (Extended Data Fig. 3). The black circles in (f) correspond to the dataset presented in (e).*

We simulated a 2D monolayer of cells constitutively expressing a fluorescent protein by initialising populations of cells whose length and fluorescence intensity were drawn from distributions obtained

from experimental data (Extended Data Fig. 1). Following initialization, we simulated cell movement by numerically integrating the equations of motion for each rod. Once the system had reached steady-state, we extracted measurements of rod position, orientation, fluorescence and length at evenly spaced timepoints. To simulate noisy measurements, we added Gaussian noise to each of these features, with the noise magnitude based on that observed in real experimental data (Fig. 3b, Methods).

Rather than specialising on datasets with specific properties, FAST's tracking algorithm is designed to be robust to a wide diversity of different conditions by automatically compensating via feature normalization. To test this capability, we varied the parameters of our simulation by adjusting the rod density, self-propulsion force and framerate, as well as the accuracy of feature measurement by adjusting the amount of noise in the measured cell position, length and fluorescence intensity. We tested five different values for each of these six parameters, yielding a total of 30 datasets in total.

The performance of the tracking algorithm was assessed by comparing its output to the ground truth (Fig. 3c,d). Links that were present in the ground truth but missing in the reconstructions were scored as false negatives (FN), while those that were absent in the ground truth but present in the reconstructions were scored as false positives (FP). Links that were identical in both were scored as true positives (TP). We now integrated these measurements into a single metric that quantifies tracking performance, the F_1-score, defined as:

$$F_1 = \frac{2\,TP}{2\,TP\ +\ FN\ +\ FP}. \tag{4}$$

Users of FAST specify a tracking threshold that controls the stringency of the linking process. If this threshold is too stringent, too many correct links will rejected by the algorithm, while if the threshold is not stringent enough too many incorrect links will be accepted. In practice, users need the ability to choose the tracking threshold that best suits their needs - for example, users interested in detecting very rare events will have different requirements than those interested in measuring average cell behaviour. However, for the purpose of testing the benefits of our automated tracking algorithm, we removed the tracking threshold as a factor from our analyses by using the threshold that resulted in the largest the F_1-score for each dataset (Fig. 3e). This greatest F_1-score is an objective measure of the performance of our tracking algorithm across datasets with different characteristics, and also allows us to robustly benchmark our tracking algorithm.

The simulated datasets were tracked using two different methods (Fig. 3b). The first method only used the position of the rods – effectively a classical position-based tracking approach ('Centroids'), while the second method used all four features – position, orientation, length and fluorescence intensity ('All features'). We found that including all features led to a dramatic increase in tracking accuracy in all datasets, with a 4 to 10-fold reduction in the number of tracking errors (Extended Data Fig. 2). Furthermore, our groundtruthed datasets allow us to directly relate a data set's trackability to the accuracy of the resulting tracks, showing that it is an excellent predictor of the F_1-score regardless of the simulation parameters or level of noise in the dataset (Fig. 3f).

Taken together, these analyses validate our methodology and illustrate how FAST copes with challenging data sets. First, they demonstrate that our method of integrating additional feature information during tracking is reliable and effective, allowing FAST to substantially reduce tracking errors compared to alternative approaches that use cell position alone. Second, these analyses demonstrate that our trackability score is able to integrate multiple aspects of the dataset into a single, robust heuristic of predicted tracking accuracy. Finally, we note the tracking algorithm used by FAST

is fully automated and requires the user to choose only a single parameter (the tracking threshold) no matter the number of different features that are used in the tracking algorithm.

Case studies

Quantifying rapid bursts of cell movement in densely packed *P. aeruginosa* monolayers

Many different species of bacteria generate collective motility in densely-packed communities using either flagella, Type IV pili, or via gliding[10,19,33,34]. Motility allows populations to rapidly expand into new territory, giving them a competitive advantage over non-motile genotypes[9,35]. Here we demonstrate how FAST can be used to quantify the behaviour of *P. aeruginosa* cells in interstitial colonies that form between agar and glass[34]. We focus on cells within the monolayer that forms directly behind the colony's leading edge, the dynamics of which play a crucial role in the competition between genotypes in both interstitial and more classical "surficial" colonies[9].

Tracking cells undergoing collective movement requires a much larger acquisition frame rate compared to non-motile cells. While expensive timing boards can be used to "trigger" cameras with a high level of precision to keep the time between frames nearly constant, most high-end research microscopes lack this capability. Instead, "camera streaming" is more widely available, which directly streams the camera's output to a computer which saves frames as fast as possible. This maximises the frame rate, but images acquired via camera streaming can have slight variations in the time that elapses between subsequent frames.

To illustrate how FAST can be used to handle a sequence of images collected via camera streaming, we collected a large dataset with 3,505 frames recorded at an average rate of 127 frames per second. The size is of this dataset is approximately 8 Gb and each frame contains approximately 1,700 tightly packed *P. aeruginosa* cells. Despite the large size of this dataset, processing with FAST could be completed on a standard laptop computer (Methods), requiring only 200 mins to segment and 355 mins to extract the features of each of the ~6 million individual objects.

Tracking consists of two separate stages: the model training stage, and the link assignment stage. After completion of the model training stage, FAST automatically generates and plots the trackability of the dataset at each timepoint (Fig. 4a). For our dataset, this plot revealed that the trackability dropped precipitously at some timepoints. We hypothesised that these decreases resulted from a reduction in the imaging framerate. To test this, we plotted the trackability score against Δt, the elapsed time between frames as calculated from timestamps (Fig. 4a, inset). This revealed a strong negative correlation (Pearson's correlation coefficient = -0.705), suggesting that the longer the time between frames, the lower the trackability and the less accurate the tracking results. To avoid these timepoints - and the spurious tracking results they might generate - we used the tracking module's built-in time window selection tool to specify a subset of frames to track (Fig. 4a, green region, 750 frames). Training the tracking model for this reduced dataset took 18 minutes, while tracking and track processing took an additional 88 minutes.

In this example, a relatively large timestep Δt allows cells to move further between frames, which reduces predictability and therefore reduces the trackability score. More generally, however, the trackability depends on a combination of experimental and imaging conditions, providing a robust metric to interpret datasets. For example, the trackability score can be used to quickly identify a wide

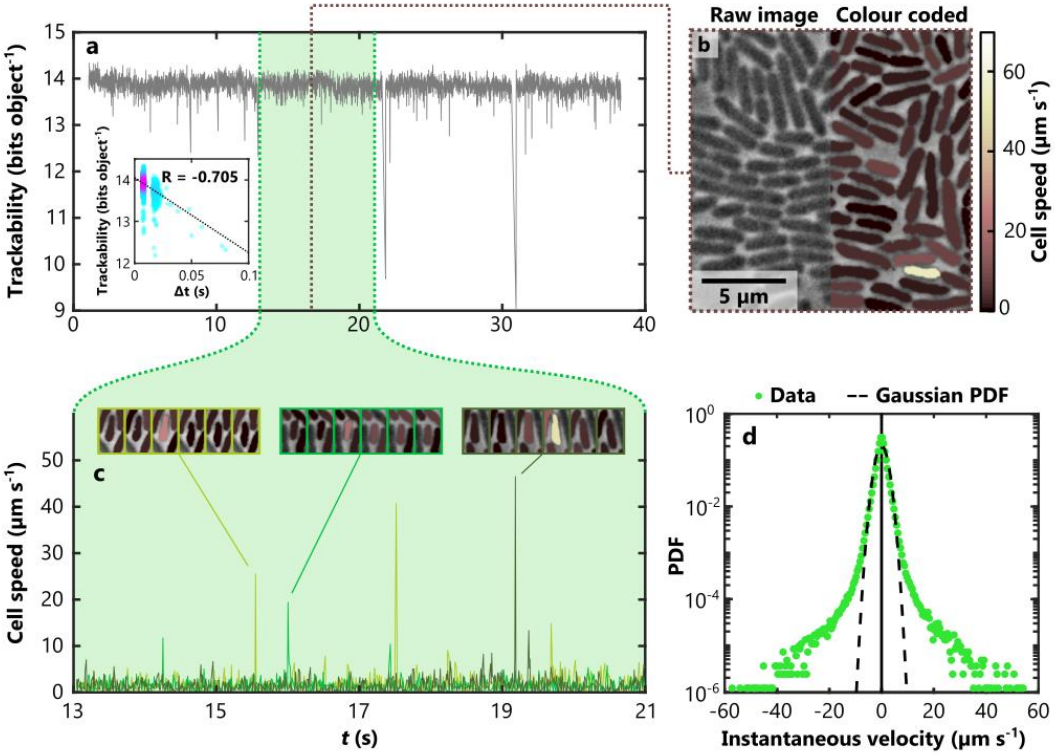

Fig. 4 | Tracking single cells in an interstitial* P. aeruginosa *colony spreading via pili-based motility. *(a) We used FAST to track cells within a monolayer of* P. aeruginosa *undergoing collective motility using position, length and width as features. Images were collected using high speed "camera streaming" with a mean frame rate of 127 fps, but variations in the elapsed time between subsequent frames, Δt, resulted in transient reductions in trackability. (a, inset) Analysis of the timestamps associated with each frame revealed that the trackability score was negatively correlated with Δt (R indicates Pearson's correlation coefficient; the warmer colours denote a higher density of data points). We therefore restricted our subsequent analyses to a subset of the data in which the trackability score was relatively constant (green region) using FAST's built-in tools. (b) We used the Overlays module to colour code cells based on their instantaneous speed. Although cells typically moved relatively slowly, very occasionally cells were observed to undergo a very rapid burst of movement (see cream coloured cell). (c) These rapid jumps can also be observed in traces of the speed of individual cells. Here we plot the instantaneous speed of three different cells over time, each in a different colour. The montages above illustrate three of these transient events, using the same colour coding shown in b. (d) To investigate these movements at the population level, we calculated instantaneous cell velocities in both the x and y direction for all cells and plotted their combined distribution. In other active systems, this distribution is approximately Gaussian[33,37]. However, in our system the highly transient bursts of velocity results in heavy tails, causing them deviate from a Gaussian distribution with the same variance (dashed black line).*

range of problems which might arise during an experiment, including fluctuations in focus, illumination intensity, or inadvertent movement of the sample. Once problematic timepoints have been identified, the user can decide either to avoid them by using a subset of the images (as in this example) or to reject the entire dataset.

Tracking the smaller subset of images that we specified resulted in over 1,600 separate trajectories, each at least 200 timepoints long. To visualise this large dataset, we used the Overlays module to colour individual cells in the phase-contrast image based on their instantaneous speed (Fig. 4b). This revealed that while most cells move at relatively slow speeds, a small number of cells undergo rapid, sporadic bursts of movement approximately 25 times faster than the average. These rapid movements are also clearly visible in measurements of the speed of individual cells over time (Fig. 4c). Our results are similar to the 'slingshots' previously observed in solitary *P. aeruginosa* cells moving at the glass/liquid interface, apparently driven by pilus detachment events[36]. However, the peak speeds that we record (up to 60 µm s^{-1}) in collectives of *P. aeruginosa* are approximately 20 times larger than those previously observed. While we do not know the specific reason for this difference, interactions with

353 neighbouring cells facilitated by the high cell density, the glass/agar interstitial colony environment
354 and our higher framerate (~13 times that of [36]) may each play a role.

355 To illustrate how this large tracking dataset can be mined to elucidate the statistics of rare events, we
356 constructed the instantaneous marginal velocity distribution from our tracks (*i.e.* the x- and y-
357 components of the instantaneous velocity vectors) (Fig. 4d). While previous studies have found that
358 sperm and swimming bacterial cells undergoing collective movement generate marginal velocity
359 distributions that are approximately Gaussian[33,37], we observed that bacteria collectively moving via
360 pili-based motility exhibit much heavier tails corresponding to their occasional rapid motions. Despite
361 the rarity of these events – less than 0.05% of our measurements had a magnitude larger than 20 µm
362 s^{-1} - the exceptional number of cell trajectories we obtained nevertheless allowed us to finely resolve
363 their statistical distribution. These analyses demonstrate how FAST can be used to rapidly characterise
364 the motility of a large number of cells in densely-packed conditions, with relatively little user input
365 and computational effort.

366 Lineage analysis of *Escherichia coli*

367 A major aim of a number previous software packages has been to automatically reconstruct cell
368 lineages[5,8]. However, identifying cell division events and the resulting daughter cells is a particularly
369 difficult challenge. Near-perfect tracking of individuals is essential for accurate lineage tracking, as a
370 single error can propagate through multiple division events, often contaminating the remainder of the
371 dataset. We decided to test FAST's lineage tracking capabilities using a time lapse movie of dividing *E.*
372 *coli* cells[17] imaged using phase-contrast microscopy. Although the tracking algorithm performed well,
373 several links were incorrectly assigned – this was particularly problematic at the beginning of the
374 dataset, because the small number of cells provided insufficient data to adequately train the machine
375 learning model. We therefore performed manual correction of the dataset using FAST's built-in track
376 validation and correction system, which required us to break 21 incorrect links and form 17 new links.
377 These manual corrections constituted only 0.67% of the 5,698 links in the final dataset, with the
378 remainder of links being correctly assigned automatically.

379 Following automated division detection, we visualised the lineage structure of the colony using the
380 Overlays module (Fig. 5a, b, Supplementary Video 1), allowing us to rapidly verify the accuracy of the
381 lineage assignment. Visualisation of the population structure revealed that the descendants of each
382 of the individual cells present at the beginning of the experiment formed highly elongated structures
383 within the colony, similar to the patterns previously observed in experiments where colonies were
384 initiated from multiple founder cells labelled with different fluorescent proteins[14]. We also used the
385 feature extraction and plotting modules to reconstruct the length of individual cells and align them by
386 the time that they last underwent division (Fig. 5c). These analyses illustrate the power and accuracy

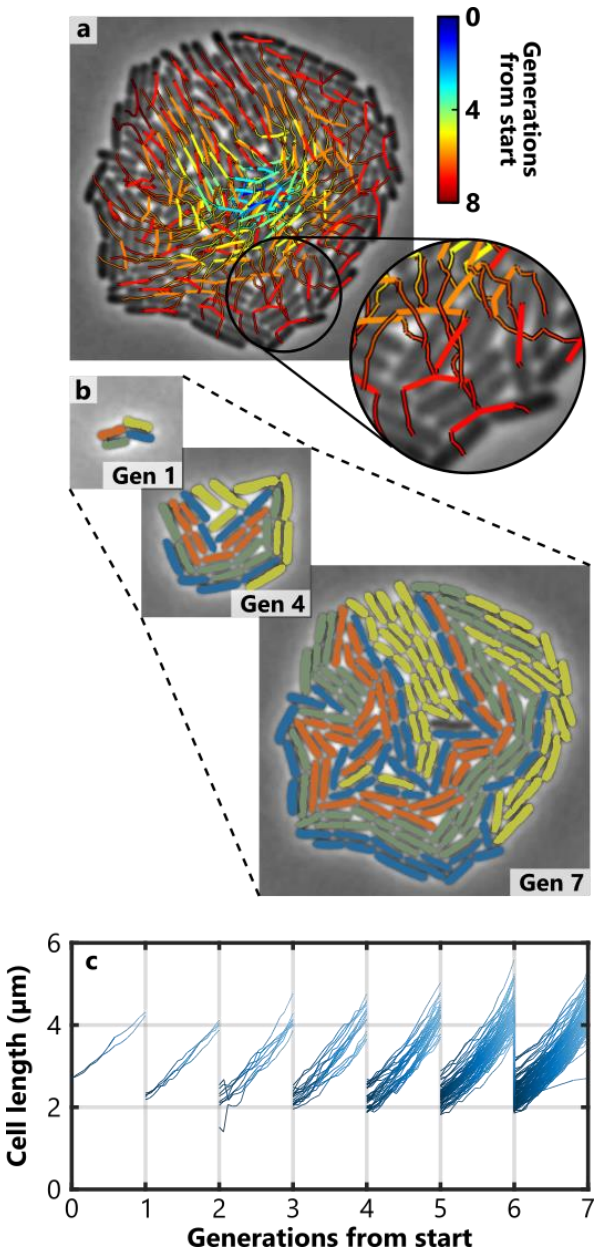

Fig. 5 | Tracking and lineage analysis of* E. coli *cells in a growing colony. *(a) Lineage tree showing the colony at the final point of the timeseries. Here thicker lines show the location of division events and thinner lines show the movement of cells between divisions. The trajectory colour indicates how many generations have elapsed in each lineage from the initial timepoint. (b) The colony at three different timepoints. Cells that share the same mother in generation 1 ('Gen 1') are shown in the same colour at each timepoint, illustrating how the spatial distribution of different lineages develops over time. (c) Growth curves of each cell, aligned by generation number. Tracks are shaded according to the age of the corresponding cell, from birth (dark blue) to division (light blue). The data visualisations of both panels a and b were produced using FAST's Overlays module, while panel c was prepared with the Plotting module.*

of our tracking and lineage reconstruction approaches, and also showcase the ease with which FAST allows data-rich visualisations of the resulting datasets.

Automated analysis of T6SS battles

To illustrate FAST's capabilities beyond standard cell tracking, we analysed the activity of the Type 6 Secretion System (T6SS) using FAST. The T6SS is a highly dynamic organelle composed of a molecular 'spear' tipped with a toxin known as an effector[38]. Bacteria that possess the T6SS can inject this effector into neighbouring cells, which kills them[39]. Firing events can be monitored by visualising the

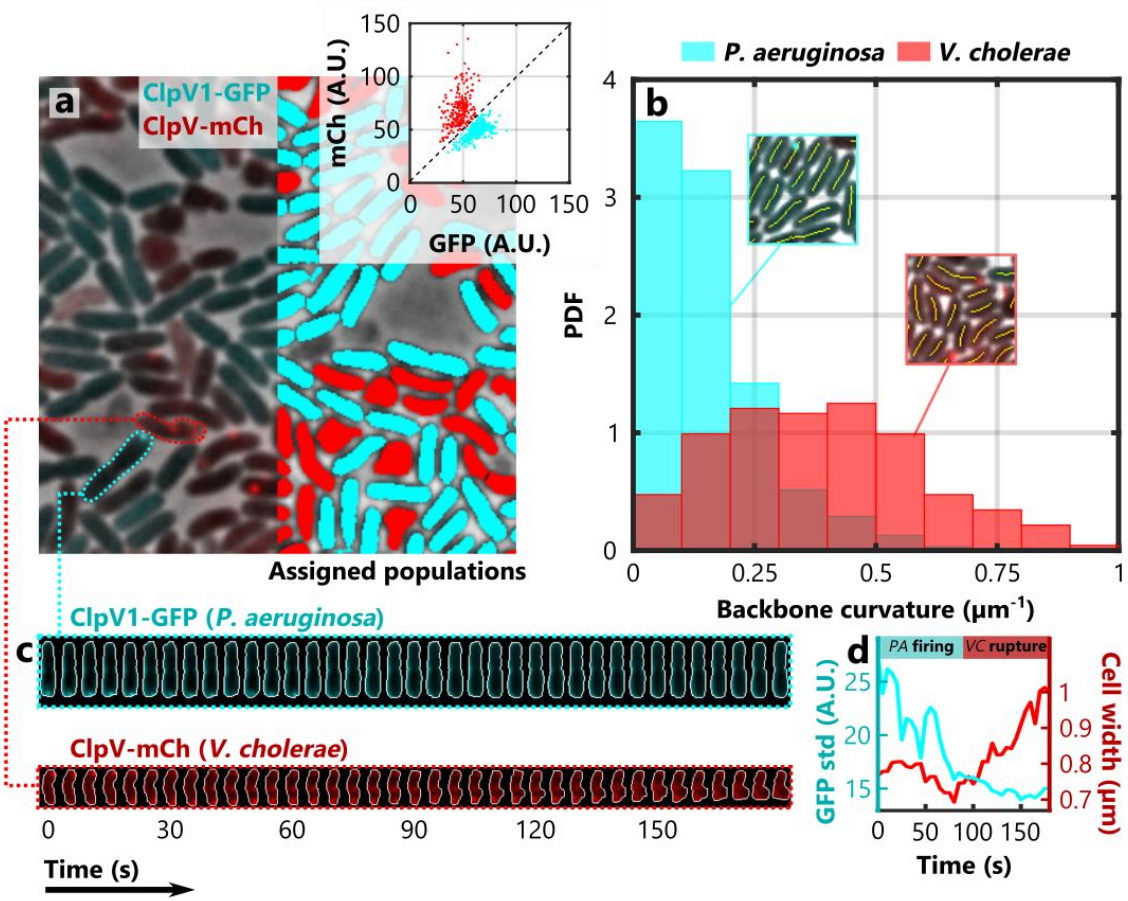

Fig. 6 | Identifying different bacterial species, quantifying cell morphologies, and investigating T6SS dynamics in a densely packed collective. *(a) A monolayer composed of a mixture of* P. aeruginosa *cells expressing GFP-ClpV1 and* V. cholerae *cells expressing mCherry-ClpV (left side). Measurements of the average intensity of each cell in the two different fluorescence channels allowed us to automatically distinguish the two species (inset), an approach known as image cytometry. By colour coding each cell (*P. aeruginosa*, cyan,* V. cholerae*, red), we were able to visually confirm the accuracy of the assignment process (right). (b) We then quantified a novel feature, cell curvature, using FAST's custom feature extraction framework. Splitting these measurements into the two previously assigned populations showed the comma shaped* V. cholerae *cells were substantially more curved than the rod-shaped* P. aeruginosa *cells. (c) We then used FAST's 'cartouche' plotting option to illustrate the dynamics of the T6SS. A* P. aeruginosa *cell (cyan) fires its T6SS machinery (observed as the bright puncta of ClpV1) at a neighbouring* V. cholerae *cell (red) which causes its wall to rupture. (d) These dynamics were captured by the features automatically quantified by FAST; the presence of the GFP-ClpV puncta in* P. aeruginosa *can be measured via the increase of the standard deviation of the GFP channel within the cell, while the rupture of the* V. cholerae *cell wall can be quantified via its rapid increase in width.*

394 localisation of ClpV, the protein responsible for disassembling the contractile sheath following
395 firing[15,40]. Here, we highlight how FAST can be used to monitor the dynamics of ClpV in a co-culture of
396 *Vibrio cholerae* and *P. aeruginosa*.

397 Because of its short range, the T6SS is effective only at high cell density, which historically has made
398 it difficult to study using automated analyses. We used FAST to analyse a dataset revealing T6SS
399 dynamics within a densely packed monolayer of cells[15]. This timeseries of images shows a mixture of
400 *V. cholerae* and *P. aeruginosa* cells expressing ClpV-mCherry and ClpV1-GFP, respectively (Fig. 6a,
401 left)[15]. We distinguished the two species from one another (Fig. 6a, right) using FAST's post-processing
402 toolbox, which compares each cell's intensity in the mCherry and GFP channels to automatically assign
403 them to two distinct populations (Fig. 6a, inset). This utility allows one to rapidly compare the
404 behaviour of different genotypes within the same sample.

405 The architecture of FAST allows users to easily define and quantify novel features that are not already
406 included in FAST. To do this, users can write a short feature measurement script that can make use of
407 the segmentation of each object in each frame, as well as the corresponding regions in each of the
408 imaging channels - in this case, the GFP, mCherry and phase-contrast signals. The Feature Extraction
409 module then automatically stores these custom features in the same way as the built-in features,
410 allowing them to be integrated into downstream analyses. To illustrate this capability, we extracted
411 cell curvature as a custom feature to see if we could detect the differences in morphology of *V. cholera*
412 cells (which are comma shaped) from that of *P. aeruginosa* (which are rod shaped). Using a
413 skeletonization-based approach, we extracted the morphological backbone of each cell from its
414 segmentation and measured its curvature by finding the best-fit circle to this set of points. Consistent
415 with expectations, our automated analysis found that the cells identified as *V. cholerae* were
416 substantially more curved than those identified as *P. aeruginosa* (Fig. 6b).

417 Our software is also capable of generating sophisticated visualisations and analyses of the behaviour
418 of single cells. We observed an event in the raw data in which a *P. aeruginosa* cell fired its T6SS
419 machinery at a neighbouring *V. cholerae* cell, causing the latter to rupture. FAST allows such dynamics
420 to be easily visualised using the 'cartouche' option in the Plotting module, which extracts and aligns
421 cropped images of a specified cell. We used this option to prepare a sequence of images that clearly
422 demonstrate the firing and rupturing behaviours of the two target cells (Fig. 6c). The feature data
423 associated with these two tracks also illustrates this effect. The firing of the T6SS can clearly be
424 observed in the *P. aeruginosa* cell at the beginning of the sequence as an increase in the standard
425 deviation of the GFP channel (caused by the formation of bright ClpV puncta within the cell), while the
426 rupture of the *V. cholerae* cell caused a rapid increase in its width (Fig. 6d). Together, this case study
427 demonstrates how FAST can automatically distinguish different species, how users can specify novel
428 features like cell curvature, and how complex bacterial behaviours can be quantified using feature
429 data.

430 Conclusion

431 Advances in experimental techniques and automated microscopy have transformed live cell imaging
432 from a technique that relies largely on qualitative observation into a highly quantitative discipline that
433 leverages huge amounts of data. Integral to this renaissance are computational tools that can
434 automatically parse and annotate the large imaging datasets resulting from these experiments. Many
435 tools have been developed for this purpose[3–8,28,41–43], each optimised for a specific research question.
436 As we have emphasized throughout this manuscript, our own contribution is particularly well-suited
437 for the analysis of experiments where cells are tightly packed together.

438 We designed FAST to allow users to rapidly obtain high-quality results by minimising both the number
439 of user-defined tracking parameters and the computational time required to process an imaging
440 dataset containing many cells. FAST automatically determines how to combine data from different cell
441 features, which prevents users from having to iteratively improve tracking results by sequentially
442 adjusting a large number of parameters – typically a very slow and laborious process. Our approach
443 also provides the user with a single, easy to interpret metric that allows them to rapidly identify and
444 avoid sections of the dataset that are predicted to yield low-fidelity trajectories. While the basic FAST
445 package already outputs most of the cell features that are widely used by researchers, simple
446 modifications to the system allow users to integrate new features into the existing analytical
447 framework.

448 Tracking systems typically break down in one of two ways – either individual objects cannot be
449 distinguished, or the tracking algorithm cannot accurately link individuals between frames. Machine

learning is increasingly used to solve the first of these two challenges, and techniques that apply machine learning methods to segment microbes at high density are now widely available[42–44]. However, use of machine learning to perform tracking is comparatively rare. FAST fills this niche using a statistical framework that both substantially improves track quality and provides users with insight into possible problems with their data. Our software has already proven its ability to elucidate the rich and complex behaviours that individual bacteria exhibit in densely-packed conditions[9,16,26,27]. Future work stemming from these combined experimental and analytical approaches could ultimately shed new light on how dense bacterial communities function and help us to develop novel strategies to manipulate them.

Materials and methods

Computational resources

All analyses presented in this manuscript were performed with a Microsoft Surface Book 2, with an 8-core Intel i7-8650U CPU and 8 Gb of RAM. FAST was run directly in Matlab, version 2018b.

SPR model

The 2D SPR model used in this manuscript has been described in detail elsewhere[9,33]. In brief, we model cells as stiff rods composed of evenly-spaced Yukawa segments, mutually repulsive point potentials. We initialise the system by filling a square domain with N_r rods, evenly spaced on a lattice. Each rod i is associated with an aspect ratio a^i and a fluorescence intensity I^i, randomly drawn from distributions fitted to the *P. aeruginosa* data from the T6SS visualisation experiment[15] as shown in Extended Data Fig. 1. The packing fraction of the system, ρ, is calculated as

$$\rho = \frac{1}{A}\sum_{i=1}^{N_r}\left[\left(a^i - 1\right) + \frac{\pi}{4}\right],$$

where A is the area of the simulated domain, which has doubly periodic boundary conditions.

Taking the instantaneous position of a rod i as $\boldsymbol{r}^i$, its orientation as ϕ^i, the unit vector denoting this orientation as $\hat{\boldsymbol{u}}^i$ and the sum of the potentials between i and all other rods as U^i, we define the equations of motion for each rod as:

$$\boldsymbol{f}_T \cdot \frac{\partial \boldsymbol{r}^i}{\partial t} = -\frac{\partial U^i}{\partial \boldsymbol{r}^i} + F\hat{\boldsymbol{u}}^i, \tag{5a}$$

$$f_\phi \frac{\partial \phi^i}{\partial t} = -\frac{\partial U^i}{\partial \phi^i}, \tag{5b}$$

where $\boldsymbol{f}_T$ is the translational friction tensor, f_θ is the rotational friction constant and F is the size of a self-propulsion force exerted by each rod along its axis. We use the formulation presented in[33] to calculate $\boldsymbol{f}_T$ and f_ϕ, which are in turn functions of the rod aspect ratio and the Stokesian friction coefficient, f_0. We simulate the dynamics of our system by numerically integrating Eq. 5a and 5b using the midpoint method.

Following an initial transient, the system reaches a statistical steady-state. At this time, we begin to measure the positions, orientations, lengths and intensities of each rod at a sampling "framerate" ΔT. We add simulated measurement noise to each of these measurements, which is drawn from a Gaussian distribution with a mean of zero. The standard deviation of the measurement noise for each feature is controlled by the parameters σ_r (positional noise), σ_ϕ (orientational noise), σ_a (length noise) and σ_I (fluorescence noise). To constrain the baseline estimates of these noise parameters, we measured how each of the corresponding features fluctuated about the mean in the *P. aeruginosa* cells of the T6SS dataset[15]. The cells in this dataset are non-motile and the framerate is high enough such that growth is negligible, meaning any apparent changes in position, orientation, length or fluorescence are wholly attributable to measurement noise.

We varied the properties of our simulations by adjusting the values of the parameters N, F, ΔT, σ_r, σ_a and σ_I in different simulation runs. The values of these parameters, as well as the fixed system parameters, are provided in table 1.

Sample preparation

The monolayer of *P. aeruginosa* presented in Fig. 4 was prepared using the wild-type PAO1 strain[45]. Cells were streaked out from freezer stocks onto LB agar plates (Lennox, 20 g/l, Fisher Scientific, solidified with 1.5% (w/v) agar, Difco brand, BD) and incubated overnight at 37°C. Single colonies were picked from the resulting plates and incubated overnight in liquid culture under continuous shaking, resulting in stationary phase cultures. These were then diluted 30-fold and returned to the shaking incubator for a further two hours, yielding cultures in exponential phase. The final culture used for inoculation was prepared by adjusting the optical density at 600 nm (OD_{600}) of the exponential phase cultures to 0.05 using fresh LB, corresponding to an approximate concentration of 12,500 cells μl^{-1}.

We prepared monolayers from these cultures using a similar protocol to that described in[34]. 1 µl of inoculation culture was spotted onto the centre of a small (2 cm x 2 cm) LB agar pad. To provide optimal conditions for observing twitching motility, the concentration of agar in these pads was 0.8%. This pad was then inverted and placed into the base of a coverslip-bottomed Petri dish (175 µm coverslip thickness, MatTek), which was then closed and incubated for 16 hr at room temperature. The ability to close the lid of the Petri dish allowed us to avoid desiccation of the sample during incubation. By the end of the incubation period, a large interstitial colony with a dense monolayer at its perimeter had formed[9].

Microscopy

The high framerate movie used for the analysis of rapid motion (Fig. 4) was acquired using a Zeiss Axio Observer.Z1 microscope outfitted with an Axiocam 702 camera set to "camera streaming" mode and a Plan Apochromat 63x oil-immersion objective.

Other datasets

The datasets showing dividing *E. coli* cells (Fig. 5) and T6SS firing (Fig. 6) were downloaded from the Supplementary Information sections of[17] and[15], respectively. FIJI's[46] built in AVI reader was used to extract individual frames of both movies. The *E. coli* movie was then stabilised using a combination of manual stabilisation (for large shifts in the field of view between timepoints) and the TurboReg plugin[47].

Acknowledgements

We would like to thank the numerous people who have tested and provided feedback on FAST during its development, including N.A. Costin, S.C. Booth, J.H. Wheeler, E.T. Granato, R.K. Kumar, W.P.J. Smith, C.J. Walther and H. Todorov. O.J.M. was supported by an EPSRC studentship through the Life Sciences Interface Centre for Doctoral Training (EP/F500394/1) and a long-term postdoctoral fellowship provided by the HFSP (LT0020/2022-L), while W.M.D was supported by a startup grant from the University of Sheffield's Imagine: Imaging Life initiative, an EPSRC Pump Priming Award (EP/M027430/1), a BBSRC New Investigator Grant (BB/R018383/1), and the Human Frontier Science Program (RGY0080/2021).

Conflict of interest

We report no conflicts of interest.

References

1. Nadell, C. D., Xavier, J. B. & Foster, K. R. The sociobiology of biofilms. *FEMS Microbiol. Rev.* **33**, 206–24 (2009).

2. Nadell, C. D., Drescher, K. & Foster, K. R. Spatial structure, cooperation and competition in biofilms. *Nat. Rev. Microbiol.* **14**, 589–600 (2016).

3. Ducret, A., Quardokus, E. M. & Brun, Y. V. MicrobeJ, a tool for high throughput bacterial cell detection and quantitative analysis. *Nat. Microbiol.* **1**, 1–7 (2016).

4. Paintdakhi, A. *et al.* Oufti: an integrated software package for high-accuracy, high-throughput quantitative microscopy analysis. *Mol. Microbiol.* **99**, 767–777 (2016).

5. Stylianidou, S., Brennan, C., Nissen, S. B., Kuwada, N. J. & Wiggins, P. A. *SuperSegger* : robust image segmentation, analysis and lineage tracking of bacterial cells. *Mol. Microbiol.* **102**, 690–700 (2016).

6. Tinevez, J.-Y. *et al.* TrackMate: An open and extensible platform for single-particle tracking. *Methods* **115**, 80–90 (2017).

7. Wang, Q., Niemi, J., Tan, C.-M., You, L. & West, M. Image segmentation and dynamic lineage analysis in single-cell fluorescence microscopy. *Cytom. Part A* **77A**, 101–110 (2009).

8. Klein, J. *et al.* TLM-tracker: Software for cell segmentation, tracking and lineage analysis in time-lapse microscopy movies. *Bioinformatics* **28**, 2276–2277 (2012).

9. Meacock, O. J., Doostmohammadi, A., Foster, K. R., Yeomans, J. M. & Durham, W. M. Bacteria solve the problem of crowding by moving slowly. *Nat. Phys.* **17**, 205–210 (2021).

10. Jeckel, H. *et al.* Learning the space-time phase diagram of bacterial swarm expansion. *PNAS* **116**, 1489–1494 (2019).

11. Granato, E. T., Meiller-Legrand, T. A. & Foster, K. R. The Evolution and Ecology of Bacterial Warfare. *Current Biology* **29**, R521–R537 (2019).

12. Smith, P. & Schuster, M. Public goods and cheating in microbes. *Current Biology* **29**, R442–R447 (2019).

13. Madsen, J. S., Burmølle, M., Hansen, L. H. & Sørensen, S. J. The interconnection between biofilm formation and horizontal gene transfer. *FEMS Immunol. Med. Microbiol.* **65**, 183–195 (2012).

14. Rudge, T. J., Federici, F., Steiner, P. J., Kan, A. & Haseloff, J. Cell polarity-driven instability generates self-organized, fractal patterning of cell layers. *ACS Synth. Biol.* **2**, 705–714 (2013).

15. Basler, M., Ho, B. T. & Mekalanos, J. J. Tit-for-Tat: Type VI Secretion System Counterattack during Bacterial Cell-Cell Interactions. *Cell* **152**, 884–894 (2013).

16. Granato, E. T. & Foster, K. R. The Evolution of Mass Cell Suicide in Bacterial Warfare. *Curr. Biol.* **30**, 1–8 (2020).

17. Nghe, P. *et al.* Microfabricated Polyacrylamide Devices for the Controlled Culture of Growing Cells and Developing Organisms. *PLoS One* **8**, e75537 (2013).

18. Kurtuldu, H., Guasto, J. S., Johnson, K. A. & Gollub, J. P. Enhancement of biomixing by swimming algal cells in two-dimensional films. *PNAS* **108**, 10391–5 (2011).

19. Jarrell, K. F. & McBride, M. J. The surprisingly diverse ways that prokaryotes move. *Nat. Rev.*

Microbiol. **6**, 466–476 (2008).

20. Zhang, H. P., Be'er, A., Florin, E.-L. & Swinney, H. L. Collective motion and density fluctuations in bacterial colonies. *PNAS* **107**, 13626–30 (2010).

21. Al-Kofahi, O. *et al.* Automated Cell Lineage Construction: A Rapid Method to Analyze Clonal Development Established with Murine Neural Progenitor Cells. *Cell Cycle* **5**, 327–335 (2006).

22. Veenman, C. J., Reinders, M. J. T. & Backer, E. Resolving motion correspondence for densely moving points. *IEEE Trans. Pattern Anal. Mach. Intell.* **23**, 54–72 (2001).

23. Meijering, E., Dzyubachyka, O., Smala, I. & van Cappellen, W. A. Tracking in cell and developmental biology. *Semin. Cell Dev. Biol.* **20**, 894–902 (2009).

24. Zhao, K. *et al.* Psl trails guide exploration and microcolony formation in Pseudomonas aeruginosa biofilms. *Nature* **497**, 388–91 (2013).

25. Luo, Y. *et al.* A hierarchical cascade of second messengers regulates Pseudomonas aeruginosa surface behaviors. *MBio* **6**, e02456-14 (2015).

26. Krishna Kumar, R. *et al.* Droplet printing reveals the importance of micron-scale structure for bacterial ecology. *Nat. Commun.* **12**, 1–12 (2021).

27. Ghosh, D. & Cheng, X. To cross or not to cross: Collective swimming of Escherichia coli under two-dimensional confinement. *Phys. Rev. Res.* **4**, 023105 (2022).

28. Hartmann, R., van Teeseling, M. C. F., Thanbichler, M. & Drescher, K. BacStalk: A comprehensive and interactive image analysis software tool for bacterial cell biology. *Mol. Microbiol.* **114**, 140–150 (2020).

29. Barry, D. J., Durkin, C. H., Abella, J. V & Way, M. Open source software for quantification of cell migration, protrusions, and fluorescence intensities. *J. Cell Biol.* **209**, 163–80 (2015).

30. Dubuis, J. O., Tkacik, G., Wieschaus, E. F., Gregor, T. & Bialek, W. Positional information, in bits. *PNAS* **110**, 16301–16308 (2013).

31. Cover, T. M. & Thomas, J. A. *Elements of Information Theory*. (John Wiley & Sons, Inc., 1991).

32. Ahmed, N. A. & Gokhale, D. V. Entropy Expressions and Their Estimators for Multivariate Distributions. *IEEE Trans. Inf. Theory* **35**, 688–692 (1989).

33. Wensink, H. H. *et al.* Meso-scale turbulence in living fluids. *PNAS* **109**, 14308–13 (2012).

34. Semmler, A. B., Whitchurch, C. B. & Mattick, J. S. A re-examination of twitching motility in Pseudomonas aeruginosa. *Microbiology* **145**, 2863–73 (1999).

35. Wei, Y. *et al.* The population dynamics of bacteria in physically structured habitats and the adaptive virtue of random motility. *PNAS* **108**, 4047–52 (2011).

36. Jin, F., Conrad, J. C., Gibiansky, M. L. & Wong, G. C. L. Bacteria use type-IV pili to slingshot on surfaces. *PNAS* **108**, 12617–22 (2011).

37. Creppy, A., Praud, O., Druart, X., Kohnke, P. L. & Plouraboué, F. Turbulence of swarming sperm. *Phys. Rev. E* **92**, 032722 (2015).

38. Hood, R. D. *et al.* A Type VI Secretion System of Pseudomonas aeruginosa Targets a Toxin to Bacteria. *Cell Host Microbe* **7**, 25–37 (2010).

39. Russell, A. B., Peterson, S. B. & Mougous, J. D. Type VI secretion system effectors: Poisons with a purpose. *Nat. Rev. Microbiol.* **12**, 137–148 (2014).

40. Basler, M. & Mekalanos, J. J. Type 6 secretion dynamics within and between bacterial cells. *Science* **337**, 815 (2012).

41. Hartmann, R. *et al.* Quantitative image analysis of microbial communities with BiofilmQ. *Nat. Microbiol.* **6**, 151–156 (2021).

42. Jeckel, H. & Drescher, K. Advances and opportunities in image analysis of bacterial cells and communities. *FEMS Microbiol. Rev.* **45**, 1–14 (2021).

43. Van Valen, D. A. *et al.* Deep Learning Automates the Quantitative Analysis of Individual Cells in Live-Cell Imaging Experiments. *PLOS Comput. Biol.* **12**, e1005177 (2016).

44. Panigrahi, S. *et al.* Misic, a general deep learning-based method for the high-throughput cell segmentation of complex bacterial communities. *Elife* **10**, e65151 (2021).

45. Bertrand, J. J., West, J. T. & Engel, J. N. Genetic Analysis of the Regulation of Type IV Pilus Function by the Chp Chemosensory System of Pseudomonas aeruginosa. *J. Bacteriol.* **192**, 994–1010 (2009).

46. Schindelin, J. *et al.* Fiji: an open-source platform for biological-image analysis. *Nat. Methods* **9**, 676–682 (2012).

47. Thévenaz, P., Ruttimann, U. E. & Unser, M. A pyramid approach to subpixel registration based on intensity. *IEEE Trans. Image Process.* **7**, 27–41 (1998).

Table 1 | Parameters of the SPR model used to generate synthetic datasets*. Here we show both range of values we tested and baseline value that was used when we varied another parameter. Note that our simulations are non-dimensionalised, using the width of a single rod as the characteristic lengthscale and the time taken for an isolated rod with $F = 1$ to move a single rod width as the characteristic timescale.*

Parameter symbol	Parameter name	Value(s)
$\boldsymbol{A}$	Area of simulation domain	10,000
$\boldsymbol{f_0}$	Stokesian friction coefficient	1
$\boldsymbol{N}$	Number of rods	700 (baseline) [300, 500, 700, 900, 1100] (variable)
$\boldsymbol{F}$	Self-propulsion force	1 (baseline) [0.7, 0.85, 1, 1.15, 1.3] (variable)
$\boldsymbol{\Delta T}$	Time between sampled timepoints	10 (baseline) [5, 7.5, 10, 12.5, 15] (variable)
$\boldsymbol{\sigma_r}$	Standard deviation of positional measurement noise	0.02 (baseline) [0.02, 0.1, 0.2, 0.4, 0.6] (variable)
$\boldsymbol{\sigma_\phi}$	Standard deviation of orientational measurement noise	0.02 radians
$\boldsymbol{\sigma_a}$	Standard deviation of length measurement noise	0.1 (baseline) [0.05, 0.1, 0.2, 0.4, 0.6] (variable)
$\boldsymbol{\sigma_I}$	Standard deviation of fluorescence measurement noise	1 A.U. (baseline) [0.5, 1, 2, 4, 6] A.U. (variable)

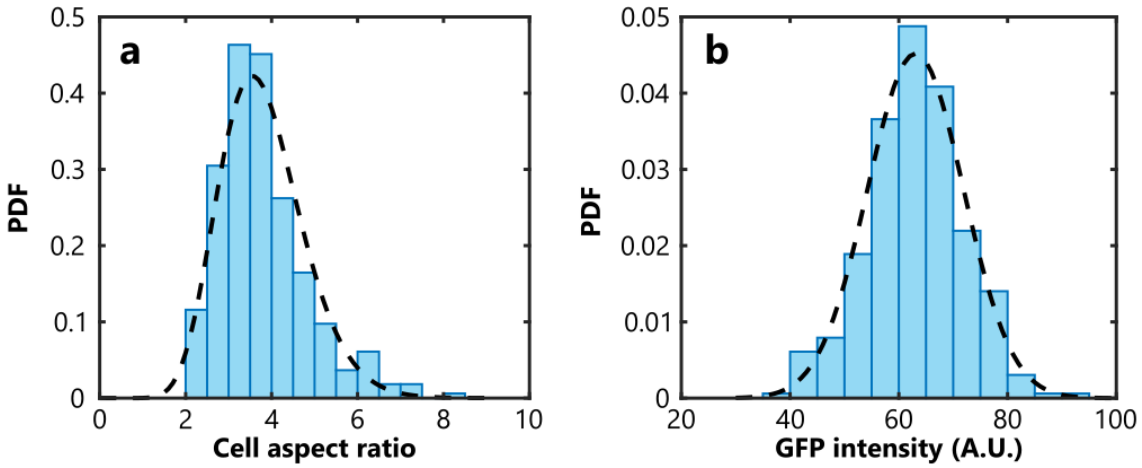

Extended Data Fig. 1 | Distributions used to specify initial conditions of the SPR model. *The distributions of trajectory-averaged aspect ratios (a) and GFP intensities (b) of the* P. aeruginosa *cells in the T6SS dataset shown in Fig. 6*[15]*. A gamma distribution (shape parameter = 15.3, scale parameter = 0.248) and a normal distribution (mean = 63.1, standard deviation = 8.83), respectively, were fitted to these two datasets (black dotted lines). To initialise the SPR model, rod aspect ratio, a_α, and simulated fluorescence intensity, I_α, were randomly drawn from these two fitted distributions, allowing us to ensure that these two features were modelled realistically in our simulations.*

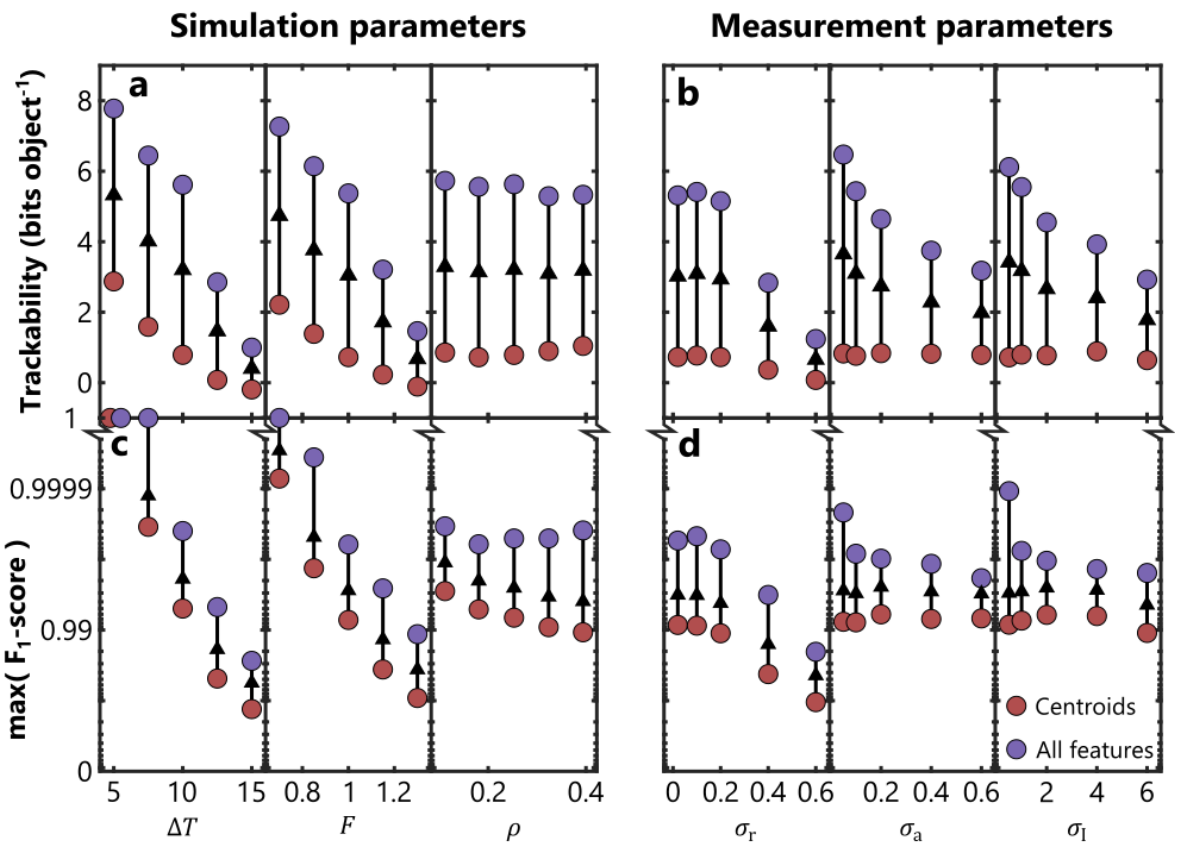

Extended Data Fig. 2 | Including additional feature information improves trackability and increases tracking fidelity. *We measured the trackability (a, b) and maximum F_1-scores (c, d) of synthetic high-density motility data generated using a range of different parameter combinations. Both 'simulation parameters' (parameters that change the properties of the SPR model we used to generate the synthetic dataset, a, c) and 'measurement parameters' (parameters that change the amount of measurement noise for each of the different features, b, d) were varied. See Table 1 for further details. Here we compare trackability and tracking fidelity when the tracking algorithm can only use positional information ('Centroids', brown) to when all feature information is available ('All features', purple). Arrows show the consistent increase in these two metrics when all features from the synthetic dataset are used, illustrating the robustness of our approach.*